The Effect of Clouds on Water Vapor Profiling from the Millimeter-Wave Radiometric Measurements

J. R. WANG, J. D. SPINHIRNE, AND P. RACETTE

Earth Sciences Directorate, NASA/Goddard Space Flight Center, Greenbelt, Maryland

L. A. CHANG

Futuretech Corporation, Gaithersburg, Maryland

W. HART

Science Systems and Applications, Inc., Lanham, Maryland

(Manuscript received 30 September 1996, in final form 21 March 1997)

ABSTRACT

Simultaneous measurements with the millimeter-wave imaging radiometer (MIR), cloud lidar system (CLS), and the MODIS airborne simulator (MAS) were made aboard the NASA ER-2 aircraft over the western Pacific Ocean on 17–18 January 1993. These measurements were used to study the effects of clouds on water vapor profile retrievals based on millimeter-wave radiometer measurements. The CLS backscatter measurements (at 0.532 and 1.064 μm) provided information on the heights and a detailed structure of cloud layers; the types of clouds could be positively identified. All 12 MAS channels (0.6–13 μm) essentially respond to all types of clouds, while the six MIR channels (89–220 GHz) show little sensitivity to cirrus clouds. The radiances from the 12-μm and 0.875-μm channels of the MAS and the 89-GHz channel of the MIR were used to gauge the performance of the retrieval of water vapor profiles from the MIR observations under cloudy conditions. It was found that, for cirrus and absorptive (liquid) clouds, better than 80% of the retrieval was convergent when one of the three criteria was satisfied; that is, the radiance at 0.875 μm is less than 100 W cm^{-3} sr^{-1}, or the brightness at 12 μm is greater than 260 K, or brightness at 89 GHz is less than 270 K (equivalent to cloud liquid water of less than 0.04 g cm^{-2}). The range of these radiances for convergent retrieval increases markedly when the condition for convergent retrieval was somewhat relaxed. The algorithm of water vapor profiling from the MIR measurements could not perform adequately over the areas of storm-related clouds that scatter radiation at millimeter wavelengths.

1. Introduction

Profiling of atmospheric water vapor with radiometric measurements near the 183.3-GHz strong water vapor line has been explored quite extensively for more than a decade (Schaerer and Wilheit 1979; Rosenkranz et al. 1982; Wang et al. 1983, 1993, 1995, 1997a; Wang and Chang 1990; Kakar 1983; Kakar and Lambrigtsen 1984; Lambrigtsen and Kakar 1995; Wilheit 1990; Lutz et al. 1991; Kuo et al. 1994). The studies by Schaerer and Wilheit (1979), Rosenkranz et al. (1982), and Kuo et al. (1994) were either theoretical or based on synthetic datasets; no real measurements were involved. The remaining studies above used radiometric measurements obtained by the airborne MIR (millimeter-wave imaging radiometer) or AMMS (airborne microwave moisture sounder). The AMMS is a four-channel (90, 183.3 $\pm$ 2, 183.3 $\pm$ 5, and 183.3 $\pm$ 9 GHz) cross-track scanner built around 1980 (Gagliano and McCheehy 1981), which has a temperature sensitivity (ΔT_b) of approximately 4 K. The MIR is a six-channel (89, 150, 183.3 $\pm$ 1, 183.3 $\pm$ 3, 183.3 $\pm$ 7, and 220 GHz), total power, cross-track scanner that was built in 1992 with a much improved ΔT_b of less than or equal to 1 K (Racette et al. 1996). Both radiometers use external calibration targets to derive the scene brightness temperature T_b. The calibration accuracy for the MIR is estimated to be better than $\pm$2 K in the T_b range of 240–300 K.

Studies made with the AMMS measurements (Lutz et al. 1991; Wang and Chang 1990; Wang et al. 1993) have shown that profiling of atmospheric water vapor profiles from radiometric measurements using the 183.3-GHz absorption line is definitely affected by the presence of a cloud cover. The retrieval was in general found to be divergent under mostly cloudy conditions

Corresponding author address: Dr. J. R. Wang, Earth Sciences Directorate, NASA/Goddard Space Flight Center, Greenbelt, MD 20771.
E-mail: wang@sensor.gsfc.nasa.gov

© 1997 American Meteorological Society

Unauthenticated | Downloaded 05/27/24 03:17 PM UTC

by these studies. It was concluded (Wang et al. 1993) that the AMMS with only four frequency channels of radiometric measurements could not provide a reliable estimation of water vapor profiles under moderately cloudy conditions. Furthermore, it was difficult to quantitatively determine the level of cloud cover (e.g., the amount of liquid water) at which the retrieval became divergent because of the poor sensitivity of the AMMS. The MIR with its improved ΔT_b and six channels of measurements may provide radiometric measurements adequate for water vapor profiling under a moderate cloud cover. Early measurements (Wang et al. 1995) with this new airborne instrument resulted in water vapor profiles that compared favorably with those measured by ground-based Raman lidar system (Whiteman et al. 1992) and rawinsondes. Comparison of coincident measurements made by the MIR and SSM/T-2 (special sensor microwave/temperature 2) aboard the DMSP (Defense Meteorological Satellite Project) *F-11* satellite during a calibration and validation program showed excellent agreement (Falcone et al. 1992). The MIR was flown a number of times together with a host of other instruments aboard the NASA ER-2 aircraft over the western Pacific Ocean during the latter part of the TOGA COARE (Tropical Ocean Global Atmosphere Coupled Ocean–Atmosphere Response Experiment) intensive observation period (IOP) of January–February 1993. Among these instruments were the cloud lidar system (CLS) (Spinhirne and Hart 1990; Spinhirne et al. 1996) and the MODIS (Moderate-Resolution Imaging Spectrometer) airborne simulator (MAS) (King et al. 1996) that could provide measurements of cloud parameters suitable for quantifying the effect of cloud on water vapor profiling by the MIR. In the following, a particular dataset obtained by these two instruments over a variety of cloud cover conditions were used to evaluate the impacts of cloud cover on water vapor retrievals from the MIR measurements

2. Measurements

The measurements used in this paper were made by the MIR, CLS, and MAS from onboard the NASA ER-2 aircraft on 17–18 January 1993. This flight is one of the many flights conducted during the last half of the TOGA COARE intensive observation period (November 1992–February 1993). The primary objective of the flight was to study convection in the region bounded by longitudes of 154°E and 158°E, and latitudes of 0 and 3°S. The aircraft was stationed in Townsville (approximately 19.4°S and 146.8°E), Australia; there was a long flight segment between the station and the region of convection, which provided a variety of cloudy conditions ideal for the current study. Figure 1 shows the flight path superimposed on the infrared image obtained by the *GMS-4* (Geostationary Meteorological Satellite) satellite. The plane took off around 2300 UTC 17 January, climbed to cruising altitude of about 19 km, and headed in a nearly straight path toward the region of convection. Between 0150 UTC and 0400 UTC it made a few east–west race track patterns over the convective region and then flew back to Townsville along nearly the same path. The whole flight took just over 8 h. This was one of several coordinated flights in which the NASA DC-8 aircraft also flew over the same region about the same time. The DC-8 aircraft was equiped with dropsonde capability and, as shown in Fig. 1, two radiosondes were dropped at locations flown over by the ER-2 aircraft. Three cloudy regions, located in the neighborhoods around 0000, 0030, and 0100 UTC along the flight path in Fig. 1, are studied in detail in the following to quantify how clouds affect water vapor retrievals based on the MIR measurements.

All three instruments (MIR, CLS, and MAS) functioned normally in the first part of the flight from Townsville to the region of convection. The characteristics of the MIR have been described in detail by Racette et al. (1996). The CLS has been flown in numerous missions in the past (Spinhirne and Hart 1990). For the TOGA COARE mission, the data system was improved and more importantly an all solid state, diode-pumped ND:YAG laser was installed. As a result of these improvements, data could be acquired for an entire 9-h flight at 7.5-m vertical, 20-m horizontal resolution at two wavelengths: 0.532 and 1.064 μm. The MAS instrument has been an evolving design. At the time of the TOGA COARE mission it was a 12-channel instrument. There were five infrared, four near-infrared, and two visible wavelength channels. Since then the instrument has been upgraded; a detailed description is given by King et al. (1996). For the current study, measurements from the 12-μm infrared and 0.87-μm visible channels of the MAS and the 1.064-μm channel of the CLS are combined to derive the optical thickness, emittance, and reflectance of the underlying atmosphere along the ER-2 flight path.

Figure 2 shows the time variations of lidar backscatter profiles recorded by the CLS between 2330 UTC and 0138 UTC, corresponding to waypoints at 148.2°E and 16.9°S, and 153.9°E and 5.1°S, respectively. The cruising altitude of the ER-2 aircraft is about 19 km, while the ocean surface is at approximately 0 km. Over regions of clear sky, a strong lidar backscatter signal from the surface is present. The three cloudy regions noted previously are further indicated in this figure as A, B, and C. The region A between 2342 and 2358 UTC is characterized by high cirrus clouds between the altitudes of 10 and 14 km. A significant lidar backscatter is observed at the surface over most of the region, suggesting that the attenuation of CLS signal in the high cloud layer is not severe and the integrated cloud water cannot be too large. Around 2348 UTC there is a small low-altitude cloud patch associated with a diminished lidar backscatter at the surface. Region B is characterized by cloud patches at altitudes below 6 km, which are likely composed of liquid water droplets. Lidar backscatter from

Unauthenticated | Downloaded 05/27/24 03:17 PM UTC

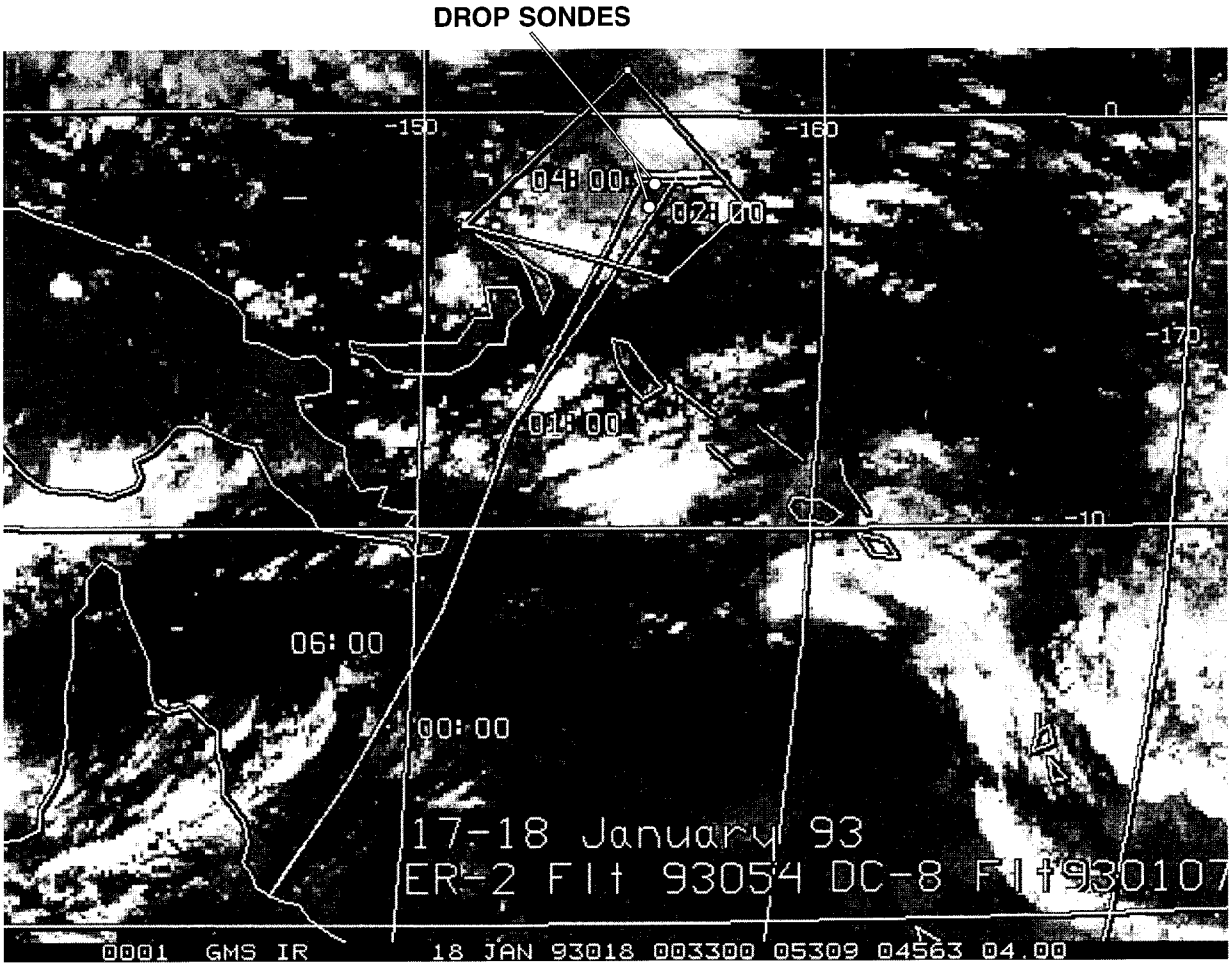

FIG. 1. The flight path of the NASA ER-2 aircraft on 17–18 January 1993 overlaying the thermal infrared image obtained by the *GMS-4* satellite.

the surface is absent in some areas. Finally, region C between the period of 0110 and 0126 UTC is characterized by optically thick clouds at a few locations. The CLS backscatter signals at the ocean surface are clearly absent at these locations. These clouds are not necessarily single-layered; some layers at low altitudes likely consist of liquid water. As shown in the next section, these locations are generally associated with high emittance, reflectance, and optical thickness; at some of these locations, the optical thickness even reaches saturation.

The responses from the visible and thermal infrared channels (at 0.875 and 12.0 μm) of the MAS over these three regions are quite different, as shown in Fig. 3. Here, the radiance $I(\lambda)$, λ being the wavelength in micrometers, from both visible and thermal infrared channels is expressed in watts per cubic centimeter per steradian. For regions A and B characterized by high cirrus and low-altitude clouds, respectively, $I(12)$ is generally greater than 4 W cm^{-3} sr^{-1}. There is a general enhancement of $I(0.875)$ in region A, but its values are less than or equal to 150 W cm^{-3} sr^{-1}. The low-altitude clouds in region B give $I(0.875)$ values as high as 300 W cm^{-3} sr^{-1}. Finally, in the center portion of the area covered by the time interval 0113–0121 UTC in region C, the $I(12)$ values fall below 2 W cm^{-3} sr^{-1} and $I(0.875)$ values reach as high as 450 W cm^{-3} sr^{-1}. The CLS profiles in Fig. 2 indicate that the clouds are multilayered, and the cloud top of the highest layer occurs near 17 km, much higher than that in region A. From the low $I(12)$ values, the clouds in the top layer appear much denser with emittance closer to unity than those of region A.

The corresponding MIR radiometric signatures, expressed in brightness temperature $T_b(\upsilon)$, at three frequency (υ) channels of 89, 150, and 220 GHz for the same ~2-h interval are displayed in Fig. 4. In region A all three channels appear insensitive to the cloud layer between 10 and 14 km. The $T_b(89)$ shows an enhancement and fluctuates in response to the low-altitude cloud patches. The response of the 89-GHz channel to the low-altitude liquid clouds is even more pronounced in region

Unauthenticated | Downloaded 05/27/24 03:17 PM UTC

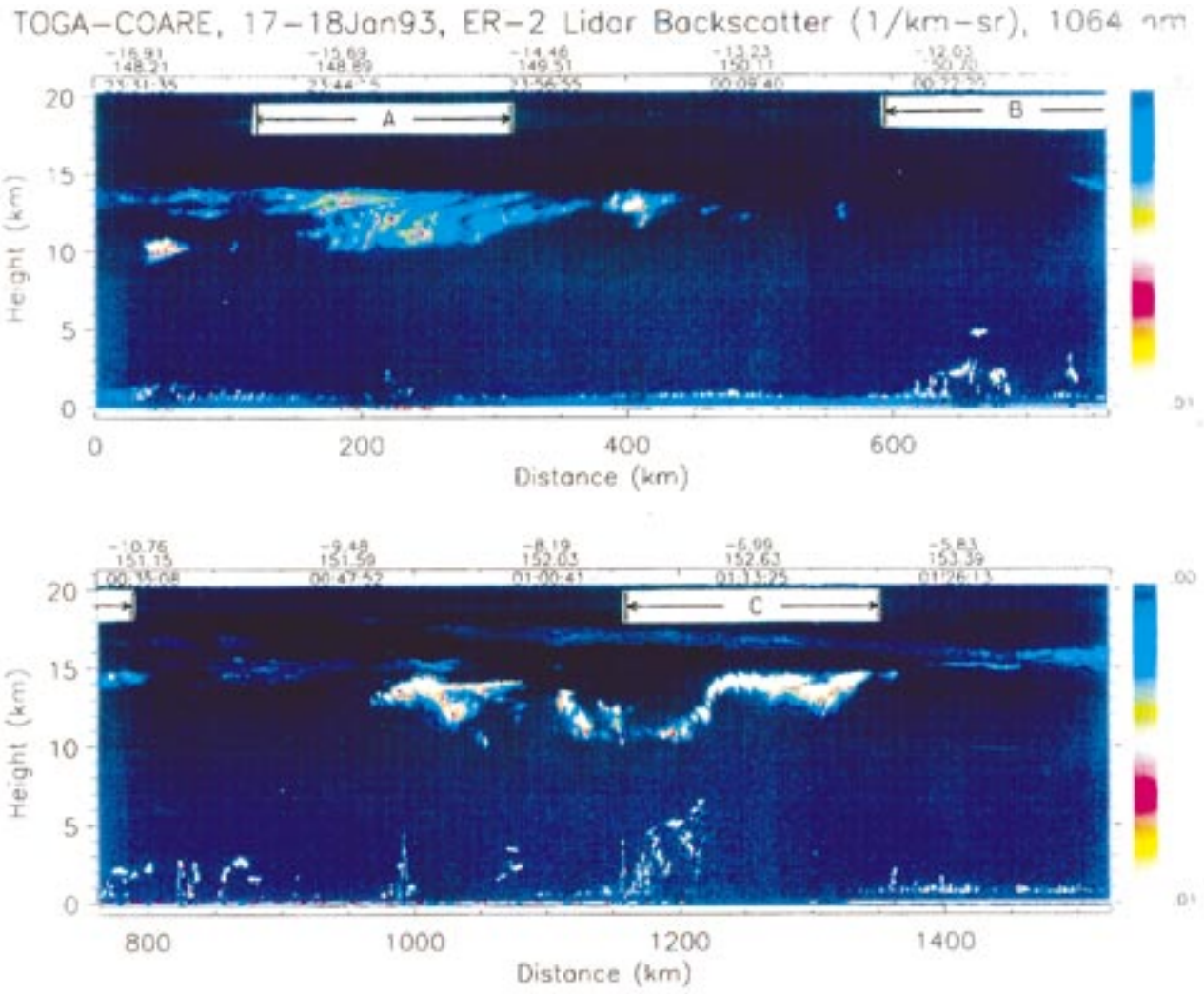

FIG. 2. The reflectivity profiles at 1.064 μm obtained by the CLS aboard the NASA ER-2 aircraft. Regions A, B, and C are characterized by cirrus clouds, low-level liquid clouds, and convective clouds, respectively.

B as $T_b(89)$ varies rapidly between 250 and 280 K. A remarkable resemblance is noted in the variational patterns of $T_b(89)$ in this figure and $I(0.875\ \mu\text{m})$ in Fig. 3. In region C the variations of $T_b(\upsilon)$ at all three channels are more complex compared to those of the regions A and B. In the starting quarter of the region, between 0111 and 0115 UTC, the variational patterns of $T_b(\upsilon)$'s are similar to those in region B; both $T_b(150)$ and $T_b(220)$ remain relatively constant while a lot of fluctuations in $T_b(89)$ occur in response to low-altitude clouds less than 6 km. After about 0116 UTC $T_b(\upsilon)$'s at all three channels decrease sharply in response to scattering of millimeter-wave radiation by atmospheric hydrometeors (Wang et al. 1997b). Both $T_b(150)$ and $T_b(220)$ recover to the values of about 282 K after 0120 UTC. Another tiny scattering cell at the time mark of about 0121 UTC causes $T_b(\upsilon)$ depressions in both 150- and 220-GHz channels. The variation of $T_b(89)$ beyond the large scattering cell (e.g., after 0120 UTC) behaves like that of region B.

Besides these apparently different features in $T_b(\upsilon)$'s displayed in the three selected regions of Fig. 4, it is also interesting to compare the $T_b(\upsilon)$ values in the clear areas of the whole region covered by the 2-h interval and infer the difference in water vapor concentrations. Note that the weighting functions at the MIR frequencies vary with altitudes depending on atmospheric moisture (Schaerer and Wilheit 1979). To facilitate discussion, the weighting functions at the MIR frequencies are calculated and displayed in Fig. 5 for two hypothetical atmospheric conditions: one extremely moist at 100% uniform relative humidity (RH) and another rather dry at 20% uniform RH. A tropical temperature profile was assumed in the derivation of these functions. The maxima of the weighting functions for the 183-GHz channels shift to higher altitudes as RH changes from 20%

Unauthenticated | Downloaded 05/27/24 03:17 PM UTC

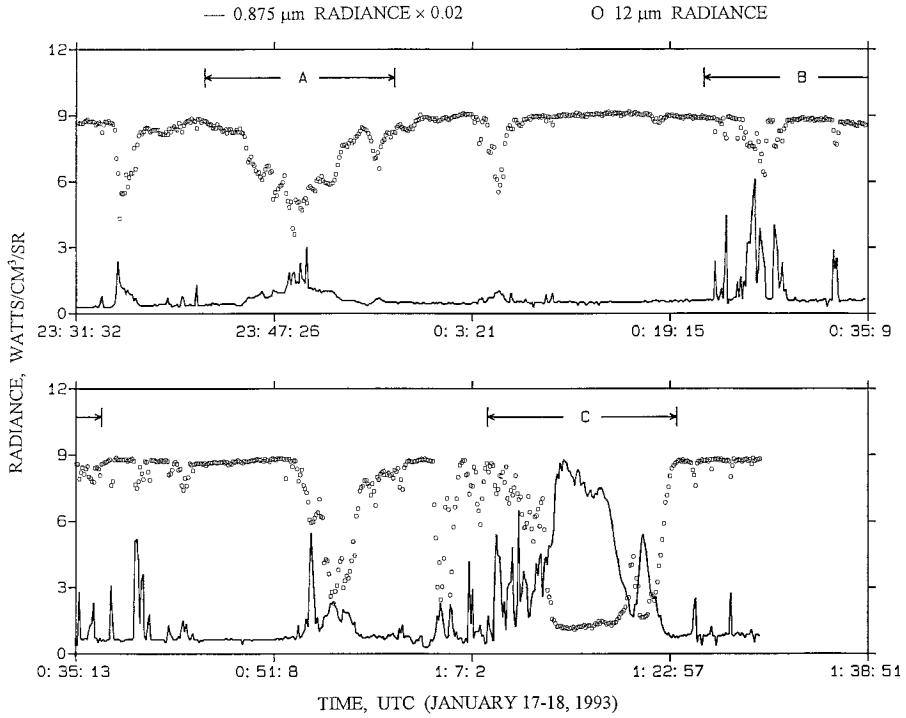

FIG. 3. The variations of radiances at 12 μm and 0.875 μm measured by the MAS aboard the ER-2 aircraft. The coverage in either time or distance is the same as that of Fig. 2.

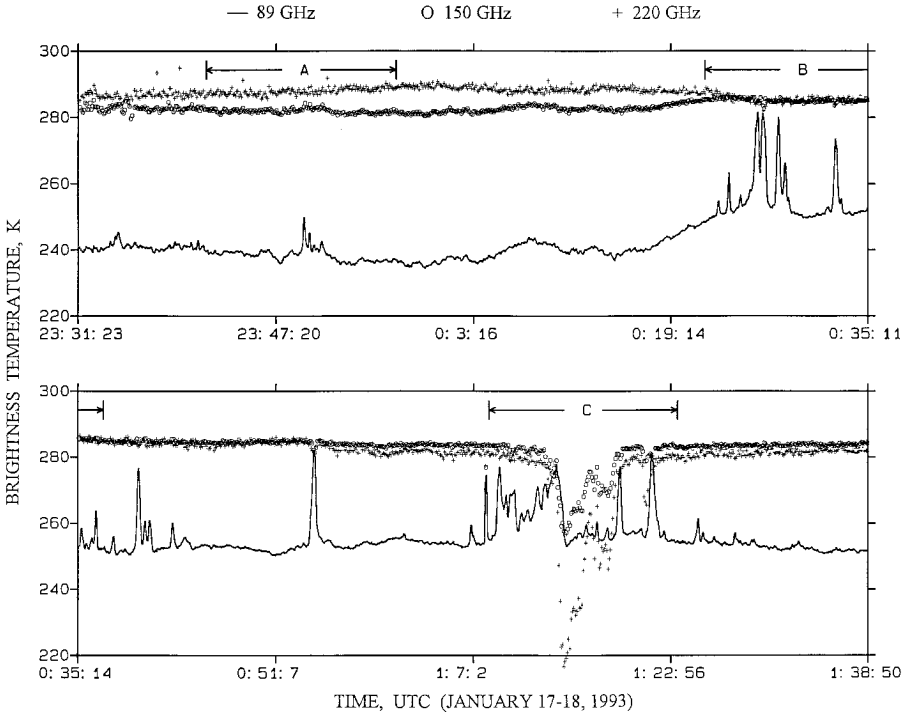

FIG. 4. The brightness temperature variations of the 89-, 150-, and 220-GHz channels of the MIR over the area covered by the CLS in Fig. 2. Notice that the 89-GHz channel is particularly sensitive to the low-level liquid clouds.

Unauthenticated | Downloaded 05/27/24 03:17 PM UTC

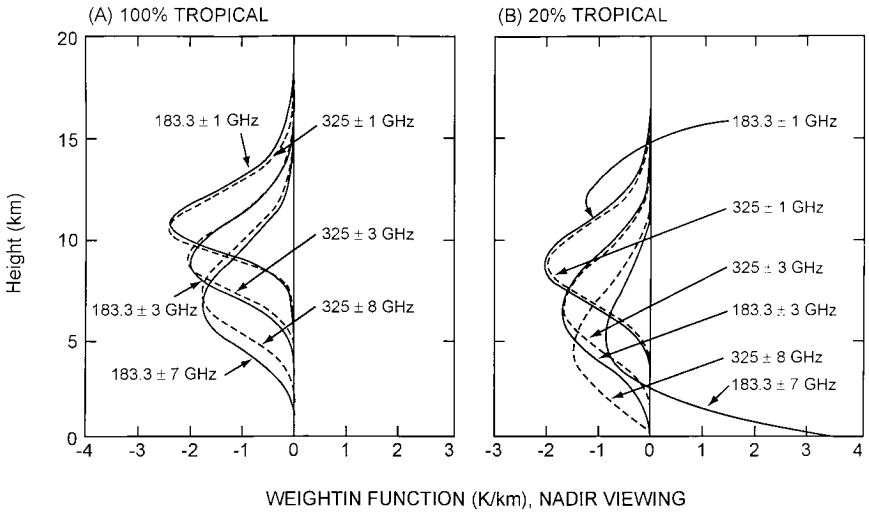

FIG. 5. Weighting functions (nadir viewing) calculated at six MIR frequencies for two hypothetical humidity profiles: (a) 20% uniform relative humidity and (b) 100% uniform relative humidity.

to 100%. At 20% RH, surface emission contributes significantly to the $T_b(\upsilon)$'s at all three window channels (89, 150, and 220 GHz); surface contribution to $T_b(183.3 \pm 7)$ is also not negligible. For tropical atmosphere with 20% uniform RH over an ocean surface, the calculated $T_b(\upsilon)$ values at $\upsilon = 183.3 \pm 1$, 183.3 ± 3, 183.3 ± 7, 89, 150, and 220 GHz are, in sequential order, 254, 270, 282, 196, 243, and 273 K. At 100% RH, these values become 237, 254, 267, 263, 283, and 276 K. There is an increase in $T_b(89)$ and a reversal in $T_b(150)$ and $T_b(220)$ as the atmosphere changes from dry to moist condition; at 20% RH, $T_b(150) < T_b(220)$, and at 100%, $T_b(150) > T_b(220)$. These trends are observed in Fig. 4. Prior to 0020 UTC on 18 January $T_b(89)$ values are less than or equal to 250 K and $T_b(150)$ is less than $T_b(220)$. This suggests that the atmosphere in this region of the ER-2 aircraft flight is only moderately moist and is slightly transparent for the 150-GHz channel to see the cold ocean surface. At times beyond 0020 UTC $T_b(89)$ greater than or equal to 250 K and $T_b(150)$ is greater than or equal to $T_b(220)$. The atmosphere in this region is quite moist and is probably totally opaque at 150 GHz. The 89-GHz channel still sees the cold ocean surface, although the atmosphere is less transparent in this region compared to that covered by the times prior to 0020 UTC on 18 January.

The simultaneous measurements of the visible (0.875 μm) and thermal infrared (12 μm) channels of the MAS and the 1.064-μm channel of the CLS provide the means to derive physical parameters such as emittance, reflectance, and optical thickness. However, there are different types of clouds, and the derivation of these cloud parameters depends on the assumption of the cloud type. Analyses using the combined airborne CLS and visible and infrared measurements have been limited to cirrus clouds (Spinhirne and Hart 1990; Spinhirne et al. 1996). The derivation of these cloud parameters in this paper makes use of these same criteria. Therefore, only the areas with a confirmation of cloud detection by CLS at altitudes greater than or equal to 6 km are chosen for derivation of these parameters. The CLS and MAS data segments, like the one in region B, that fail to satisfy this condition are excluded from this process.

3. Water vapor profiling

The algorithm used for the retrieval of water vapor profiles from the millimeter-wave radiometric measurements has been reported in the literature (Wang and Chang 1990; Wang et al. 1983). It was applied successfully to data acquired by both AMMS and MIR (Wang et al. 1983, 1995, 1997a; Wang and Chang 1990). Therefore, only a few of its features relevant to this paper are briefly described here. The algorithm applies a physical iterative scheme in which the $T_b(\upsilon)$ values at the frequency channels of the instrument are calculated from the estimated water vapor profile and compared with the ones measured by the instrument in each iteration. This comparison is expressed as the root-mean-square of the differences between the calculated and measured $T_b(\upsilon)$ values, δT_b, as

$$\delta T_{\rm b} = \left\{ \frac{1}{n-1} \sum_{\upsilon=1}^{n} [T_{bc}(\upsilon) - T_{bm}(\upsilon)]^2 \right\}^{1/2}, \quad (1)$$

where the subscripts m and c, respectively, refer to the measured and calculated $T_b(\upsilon)$ values. An initial constant relative humidity profile of 50% is assumed to initiate the iteration. When δT_b is less than or equal to a specified quantity ε at any iteration, the retrieval is convergent and the estimated water vapor profile is considered adequate for the measured T_b values. In principle, one

Unauthenticated | Downloaded 05/27/24 03:17 PM UTC

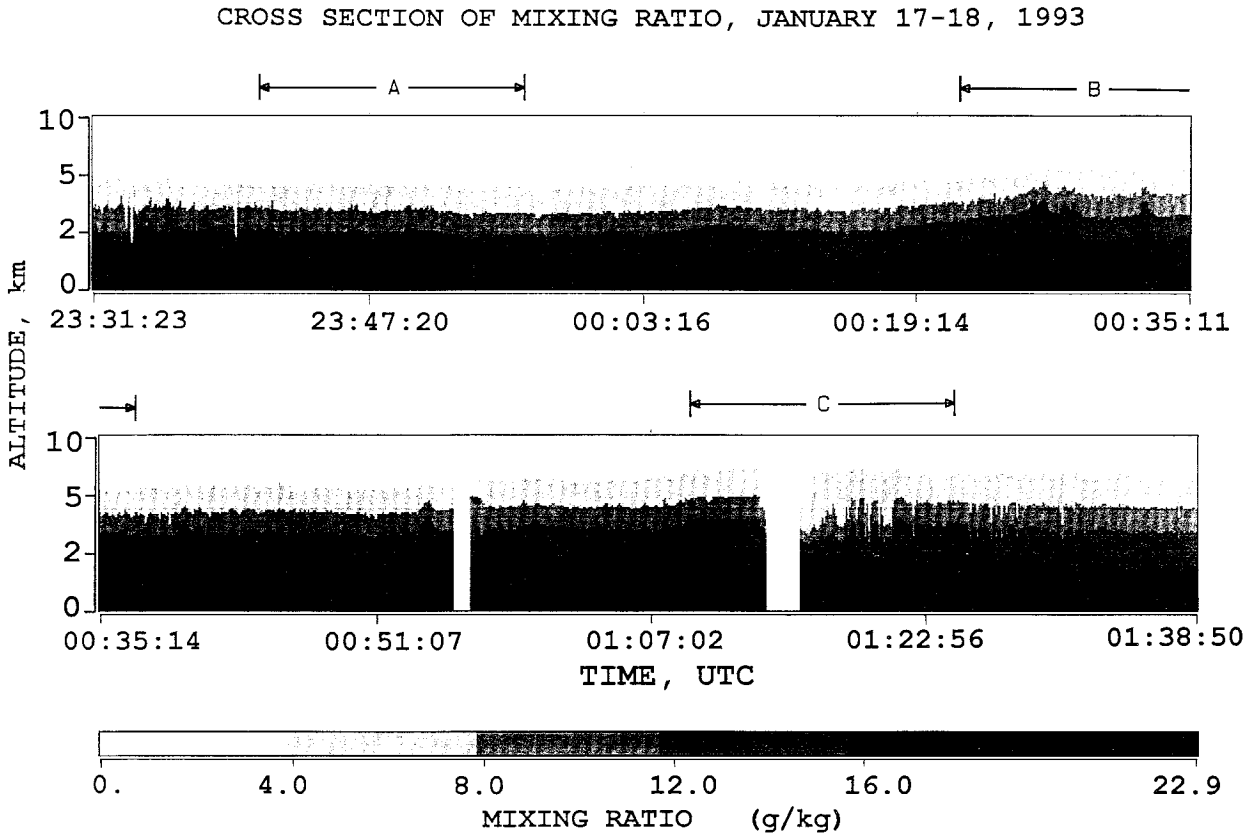

FIG. 6. The retrieved profiles of water vapor mixing ratio in gram per kilograms from the surface to 10-km altitude. Notice that, except region C of the convective cell, there is a general enhancement of water vapor with the low-level clouds.

would choose ε to be as small as possible to ensure the most accurate retrieved profiles conforming to the measurements; but a very small ε would lead to an impractical number of iterations and reduce the number of convergent retrievals from a given set of measurements (Wang et al. 1997a). Based on the accuracy of the MIR radiometric measurements of 1–2 K, ε is set to be equal to 1 K in this paper. The water vapor is retrieved at six altitudes of 0.25, 1.25, 2.25, 4.75, 7.25, and 10.25 km from the six channels of MIR measurements.

The algorithm allows for the presence of modest cloud covers. During each iteration, if the RH reaches 95% at any of the six altitude levels, a small amount of liquid water is input at that level and, in the new iteration, the T_b values are calculated again to include the effect of liquid cloud absorption. The algorithm has also been modified to take into account the revised atmospheric millimeter-wave propagation model (Liebe 1989; Liebe et al. 1991). A calm water surface is assumed for simplicity; it has been shown that the impact on water vapor profiling due to the effect of wind-roughened ocean surface on the surface emissivity is small when surface wind speed is less than or equal to 10 m s^{-1} (Wang et al. 1995). Finally, the algorithm is capable of retrieving water vapor profiles from the MIR measurements at any view angle (Wang et al. 1997a). In this paper, retrievals are made from the MIR measurements along the nadir-viewing direction only, conforming to the CLS measurements.

Figure 6 shows the water vapor profiles, in gray scale, retrieved from the MIR measurements over the entire period covered by the CLS in Fig. 2. The profiles are expressed in terms of mixing ratio ρ in gram per kilograms at different altitudes and times. The gap around 0055 UTC in the bottom panel of the figure is caused by noisy data in the 183.3-GHz channels and the retrievals are not performed. The three regions with different characteristics of cloud covers discussed in the last section are indicated in both top and bottom panels in the figure. For regions A and B the retrievals are mostly convergent. The ρ values are in the range of 15–17 g kg^{-1} near the surface and approximately 10–12 g kg^{-1} at the altitude of approximately 2 km in region A. There is a general enhancement of ρ profiles in region B when compared to those in region A. In the areas where there are clouds and $T_b(89)$ values are high, ρ values are also high. The variation of ρ in region C is more complex. First, there is a gap of about 2 min around 0114 UTC, corresponding to the area of strong depressions in both $T_b(150)$ and $T_b(220)$ (see Fig. 4), where convergent retrievals could not be obtained. For nearly 3 min after the gap, the ρ values show a lot of

Unauthenticated | Downloaded 05/27/24 03:17 PM UTC

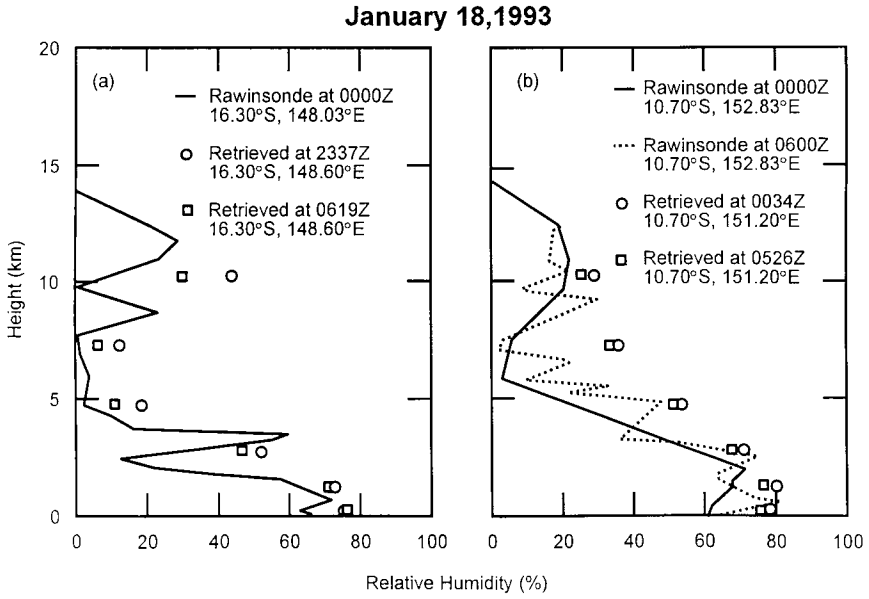

FIG. 7. A comparison of the retrieved and observed relative humidities at two different locations: (a) near 16.30°S, 148°E and (b) 10.7°S, 152°E.

fluctuations at altitudes greater than 2 km. The retrievals in this 5-min interval are divergent and to be discussed in relation to Fig. 11 below. The atmosphere is quiescent in the area corresponding to the times greater than 0122 UTC in this region and beyond, and the retrieved profiles show relatively smooth variations. The ρ values near the surface vary between 18 and 20 g kg^{-1}, and are about 15 g kg^{-1} at the altitude of 2 km. All the profiles at times greater than 0122 UTC have higher ρ values than those of region A, confirming the statement made in the previous section.

Figures 7 and 8 show a comparison of the retrieved and observed values of RH at the locations where either the dropsondes or rawinsondes are available near the times of the MIR measurements. The RH value rather than ρ is used here to enhance the detailed structure of both retrieved and observed profiles. In Figs. 7a and 7b a comparison of the retrieved and observed RH profiles

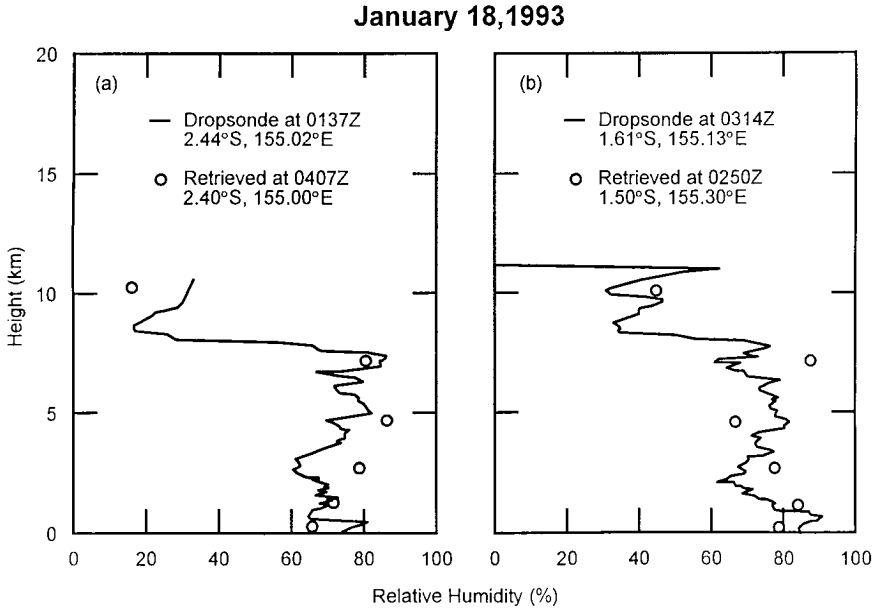

FIG. 8. A comparison of the retrieved and observed relative humidities at two different locations near the equator: (a) near 2.4°S, 155°E and (b) near 1.6°S, 155°E. The dropsonde observations were made aboard the NASA DC-8 aircraft.

Unauthenticated | Downloaded 05/27/24 03:17 PM UTC

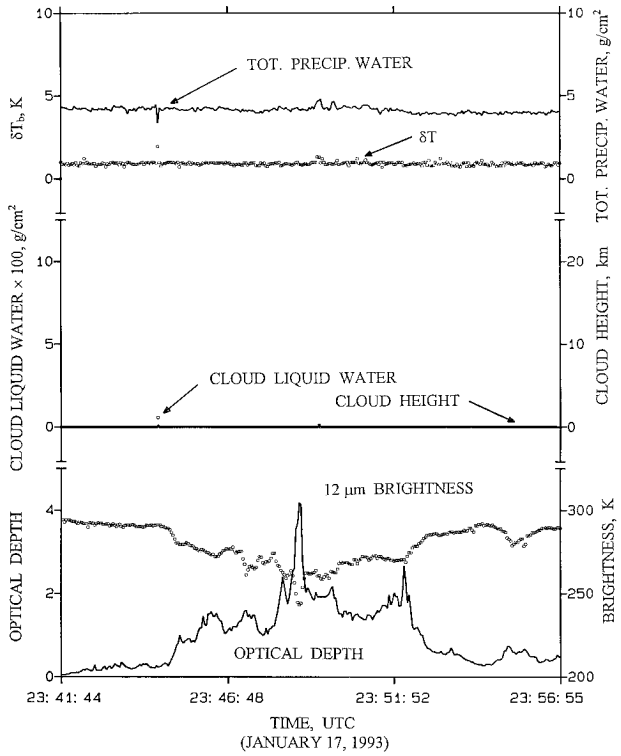

FIG. 9. The variations of the retrieved total precipitable water, condition of convergent retrieval, cloud liquid water, cloud height, optical depth, and the brightness at 12 μm in region A.

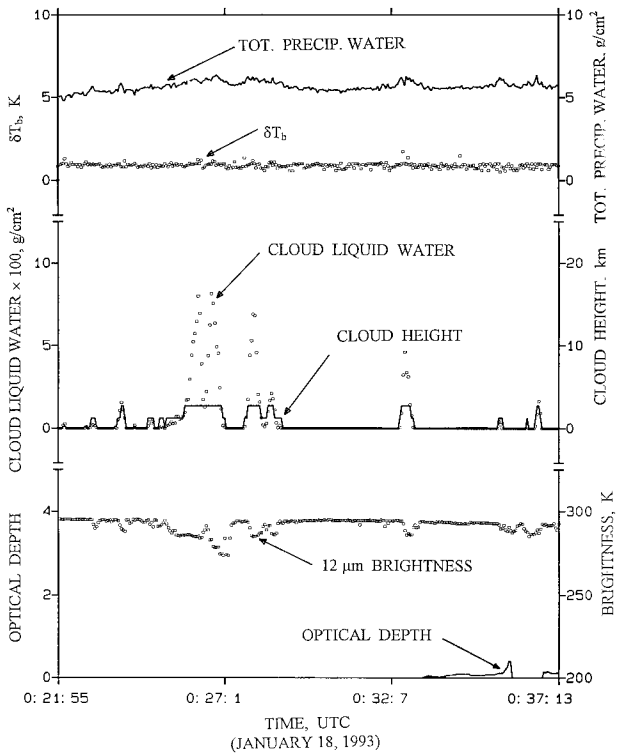

FIG. 10. The variations of the retrieved total precipitable water, condition of convergent retrieval, cloud liquid water, cloud height, optical depth, and the brightness at 12 μm in region B.

is made at two different rawinsonde stations located at 16.30°S, 148.03°E and 10.70°S, 152.83°E; the sky was relatively clear during the aircraft flight over these locations (see Fig. 1). In Figs. 8a and 8b RH profiles derived from the DC-8 aircraft dropsondes at two different locations near the equator (Fig. 1) are compared with those retrieved from the MIR measurements; the sky was cloudy in this region. The retrieved RH values are in good agreement with those observed by the dropsondes in Fig. 8 and appear to be somewhat higher than those observed by the rawinsondes in Fig. 7. Furthermore, both the retrieved and observed RH profiles show higher values near the equator than those in the latitude region of 10°–20°S, as expected. The results of this comparison and the retrieval accuracy are typical of the MIR measurements reported previously (Wang et al. 1997a).

Figures 9, 10, and 11, for regions A, B, and C, respectively (Fig. 4), compare the results of retrievals from MIR data with those from CLS and MAS. The top portion of each figure gives the total precipitable water W derived from the retrieved ρ profiles and the rms value for retrieval, δT_b. The middle portion of each figure gives the estimated cloud top and total cloud liquid water (CLW) needed for a convergent water vapor profiling from the MIR measurements. The bottom portion of each figure provides the variations of the observed T(12 μm) and the estimated optical depth τ. For region A in Fig. 9, the high cirrus and some low-altitude clouds cause the depression in T(12 μm) to as low as approximately 250 K and give rise to τ values as high as approximately 4. The W values are generally lower than 5 g cm^{-2}, and except for a few data points the δT_b's are less than or equal to 1 K, indicating satisfactory water vapor profiling throughout the region. The clouds in this region apparently have very little impact on MIR profiling of water vapor. The presence of CLW $\cong$ 0.006 g cm^{-2} at 2344 UTC is associated with nonconvergent retrieval with $\delta T_b = 1.94$. This is caused by a sporadic signal in the 220-GHz channel; there are several data points of this nature in the top panel of Fig. 4.

The results from regions B and C show significant impacts from clouds on MIR water vapor profiling. From the top portion of Fig. 10 for region B, the values of W are mostly greater than or equal to 5 g cm^{-2} and, with the exception of a few data points, δT_b less than or equal to 1 K. In the middle portion of the figure, a significant amount of CLW is needed at several places to arrive at a convergent retrieval; the estimated cloud heights are less than 3 km. The locations of these MIR-estimated cloud parameters coincide nicely with the depressions in T(12 μm) values in the bottom portion of the figure. The values of optical depth τ are not estimated in most of this region because of the criteria set on the cloud height, as discussed in the previous section. The results for region C in Fig. 11 show the difficulty of water vapor profiling using the MIR measurements.

Unauthenticated | Downloaded 05/27/24 03:17 PM UTC

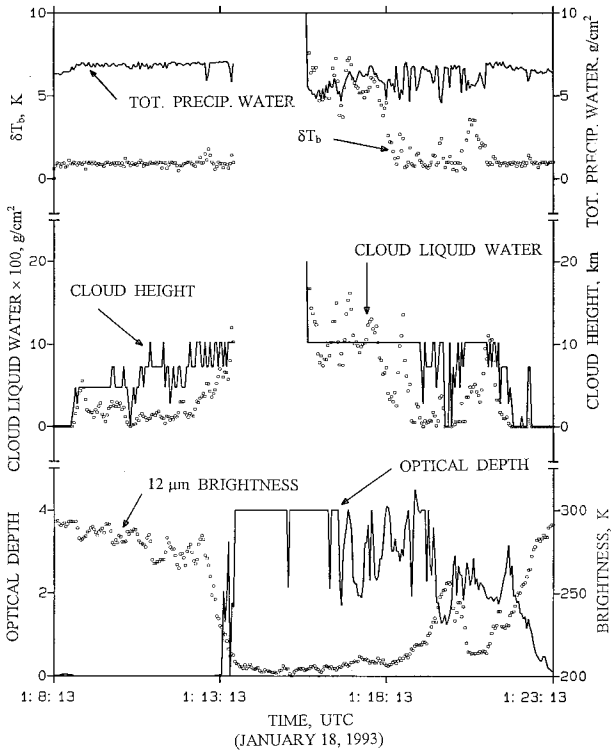

FIG. 11. The variations of the retrieved total precipitable water, condition of convergent retrieval, cloud liquid water, cloud height, optical depth, and the brightness at 12 μm in region C.

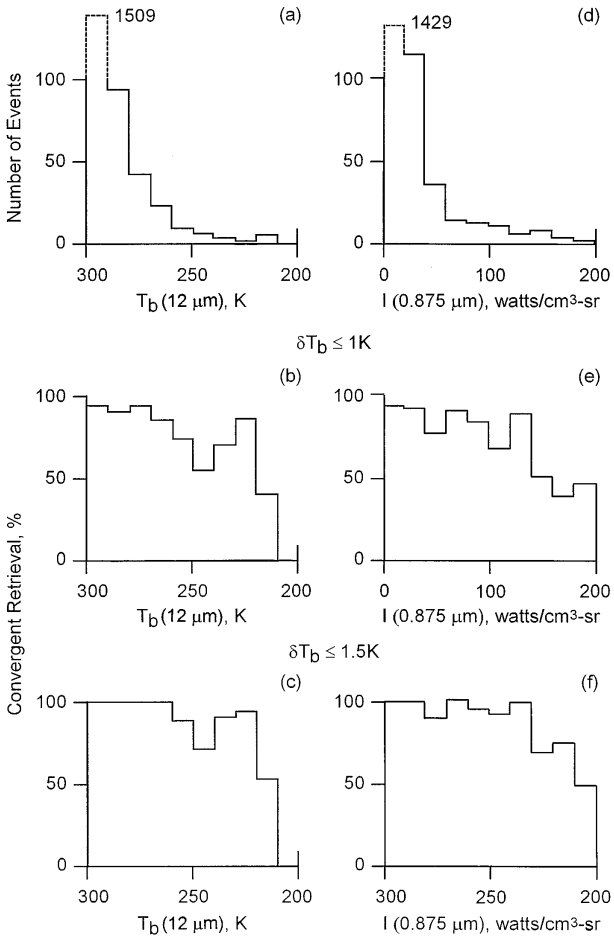

FIG. 12. Distribution of the retrieval events and the percentage of convergent retrieval using the brightness at 11 μm and radiance at 0.875 μm as classifiers. Plots (b) and (e) give results with convergent condition $\delta T_b \leq 1$ K, while plots (c) and (f) give results with $\delta T_b \leq 1.5$ K.

In the first third of the figure covering the time period of 0108–0113 UTC there is a general decrease in $T(12\ \mu\text{m})$ indicating the presence of cloud cover. After 0113 UTC $T(12\ \mu\text{m})$ decreases sharply, fluctuates between 200 and 210 K for nearly 5 min, and then gradually increases. This is followed by another depression in $T(12\ \mu\text{m})$ around 0121 UTC. The estimated τ values show saturation (which is set equal to 4 in this figure) at a number of places within the period of 0114–0120 UTC. Nonconvergent retrievals with $\delta T_b > 1$ K are obtained for the entire interval of 0114–0119 UTC, including the gap where values of the retrieved parameters are too large to be included in the figure. In the interval between 0108 and 0112 UTC convergent retrievals from MIR measurements are obtained even under the presence of cloud covers with liquid water as high as 0.08 g cm^{-2}.

4. The effects of clouds

The lidar backscatter profiles obtained by the CLS and shown in Fig. 2 provide an excellent account of the types and the detailed structure of clouds. As pointed out in section 2, however, one has to specify the cloud type to derive physical parameters such as optical depth τ, emittance e, and reflectance r from the combined measurements of CLS and MAS (Spinhirne and Hart 1990; Spinhirne et al. 1996). Thus, in the derivation of τ values for cirrus clouds, which were entered in Fig. 9, 10, and 11, only those CLS measurements with a cloud top greater than or equal to 7 km were considered. As a result, none of these physical parameters were derived for most of region B characterized by low-level clouds, as shown in Fig. 10. It is therefore not meaningful to associate these parameters with the profiling of water vapor from the MIR measurements that makes no distinction of cloud types. The radiances of clouds measured by the MAS, on the other hand, could be compared with the results of MIR water vapor profiling and help categorize the convergence of retrieval.

Figure 12 provides such a comparison for the concurrent MIR and MAS measurements, with the exception of the convective cell in region C, over the period from 2330 UTC 17 January to 0138 UTC 18 January 1993. Here, the values of radiance $I(0.875\ \mu\text{m})$ (right column of the figure) and brightness $T(12\ \mu\text{m})$ (left column of the figure) from the MAS are used to categorize the MIR measurements. The top portion of the

Unauthenticated | Downloaded 05/27/24 03:17 PM UTC

figure shows the distribution of the number of events concurrently measured by the MIR and MAS within the ranges of $I(0.875\ \mu m)$ and $T(12\ \mu m)$. The middle and bottom portions of the figure give, in each category of $I(0.875\ \mu m)$ and $T(12\ \mu m)$, the percentage of convergent retrieval of water vapor profiles based on the MIR measurements when the conditions of the convergence δT_b's are set to less than or equal to 1 K and less than or equal to 1.5 K, respectively. It is noted that more than 80% of the events occur with $T(12\ \mu m)$ greater than 270 K or $I(0.875\ \mu m)$ less than 60 W cm^{-3} sr^{-1}. Even under practically clear-sky conditions with $T(12\ \mu m)$ greater than 290 K or $I(0.875\ \mu m)$ less than 20 W cm^{-3} sr^{-1}, there is about 5% of nonconvergent events when $\delta T_b \leq 1$ K; these events disappear when $\delta T_b \leq 1.5$ K. These clear-sky, nonconvergent events can be attributed to measurement noise such as that displayed by some data points in the 220-GHz channel in Fig. 4. Based on the distribution of Fig. 12, it appears that adequate water vapor profiling can be performed from the MIR measurements when $T(12\ \mu m)$ is greater than 250 K or $I(0.875\ \mu m)$ is less than 100 W cm^{-3} sr^{-1}. When the condition of convergent retrieval is relaxed to $\delta T_b \leq 1.5$ K, adequate water vapor profiling can be obtained with $T(12\ \mu m)$ greater than 220 K or $I(0.875\ \mu m)$ less than 140 W cm^{-3} sr^{-1}. It is noted that there are not many events with either $I(0.875\ \mu m)$ greater than 100 W cm^{-3} sr^{-1} or $T(12\ \mu m)$ less than 250 K. Analysis with more concurrent measurements from these instruments is needed to arrive at a firm conclusion.

An examination of Fig. 4 clearly indicates that the 89-GHz channel is particularly sensitive to the low-level liquid clouds over the ocean surface. It is therefore interesting to examine the relation between the convergent retrievals and the $T_b(89)$ values. Figure 13a shows the frequency distribution of MIR measurements based on the categories of $T_b(89)$ values in 10-K steps from 230 to 290 K. Again, the events associated with the scattering cell in region C (Fig. 4) are not included in the figure. Figures 13b and 13c, respectively, give the percentage of convergent retrievals within each category when the conditions of $\delta T_b \leq 1$ K and $\delta T_b \leq 1.5$ K are applied. It is clear that profiling of water vapor under cloudy condition begins to deteriorate only when $T_b(89) \geq 270$ K. If the condition for convergent retrieval is relaxed to $\delta T_b \leq 1.5$ K, then the histogram of Fig. 13c suggests a better than 80% of convergent water vapor profiling from the MIR measurements under a variety of absorptive clouds.

It is also interesting to look at the dependence of $T_b(89)$ on the total cloud liquid water required by the algorithm to satisfy a convergent retrieval of water vapor profile. Figure 14 shows the scatterplot between $T_b(89)$ and the estimated CLW from the retrieval algorithm. The data points on the vertical axis correspond to clear-sky condition as viewed by the MIR. Generally, there is a nonlinear dependence of $T_b(89)$ on CLW and

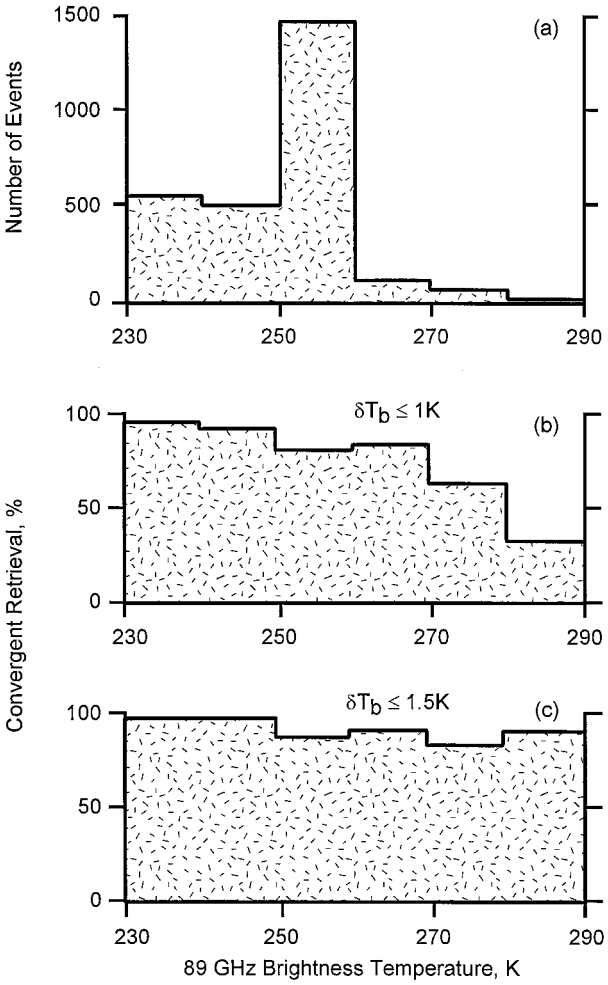

FIG. 13. Distribution of the retrieval events and the percentage of convergent retrieval using the MIR 89-GHz brightness as the classifier. Plots (b) and (c) give results with convergent conditions $\delta T_b \leq 1$ K and $\delta T_b \leq 1.5$ K, respectively.

$T_b(89)$ reaches a saturated value of about 280 K at CLW ≥ 0.09 g cm^{-2}. These estimated CLWs are not validated; they are the by-product of the MIR water vapor profiling. Their usefulness needs to be explored in the future.

5. Conclusions

During January–February 1993 a host of instruments were placed aboard the NASA ER-2 aircraft, which made a number of observations over a region in the western Pacific Ocean in support of the TOGA COARE mission. Among these instruments were MIR, CLS, and MAS, whose simultaneous measurements were analyzed to study the effects of clouds on water vapor profiling from the radiances observed at the millimeter wavelengths. The measurements for this particular study were obtained from a long flight segment covering a region stretching from near Townsville, Australia, where the aircraft was stationed, to a waypoint near the equator

Unauthenticated | Downloaded 05/27/24 03:17 PM UTC

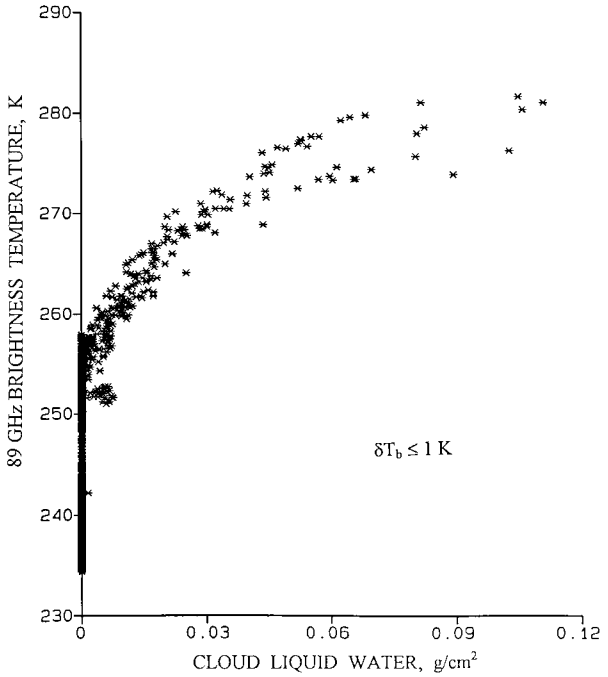

FIG. 14. The scatterplot of the measured 89-GHz brightness temperature and the cloud liquid water estimated in the retrieval process.

on 17–18 January 1993. All three instruments functioned well over the 2-h plus interval and made observations over a variety of clouds, both scattering and absorptive in the millimeter wavelengths. There were a total of 2377 events with simultaneous measurements from the three instruments. A retrieval algorithm was applied to the nadir-viewing measurements from the MIR to estimate profiles of water vapor mixing ratio along the flight segment. It was found that the estimated profiles showed a general enhancement from high latitude to equatorial region as expected. Normal retrievals could be performed from the MIR measurements over the areas of cirrus clouds or moderate liquid clouds. Over the areas of heavy cloud covers with the presence of atmospheric hydrometeors that scatter radiation at the MIR frequencies, retrievals would experience difficulty and the estimated water vapor profiles became unreliable.

All six channels of the MIR measurements show little sensitivity to cirrus clouds from this flight; they all respond to convective clouds. The 89-GHz channel shows most sensitivity to the absorptive (liquid) clouds. To quantify the effects of absorptive clouds on the water vapor profiling from the MIR radiometric measurements, radiances obtained by the 12-μm and 0.875-μm channels of the MAS and the 89-GHz channel of the MIR were used as classifiers. It was found that more than 80% of the retrieval of water vapor profiles from the MIR measurements was convergent (defined as the root-mean-square value of the measured and calculated brightness temperatures $\delta T_b \leq 1$ K) when the brightness at 12 μm was greater than or equal to 260, or the radiance at 0.875 μm less than or equal to 100 W cm^{-3} sr^{-1}, or the brightness at 89 GHz less than or equal to 270 K. When the condition of convergent retrieval was relaxed to $\delta T_b \leq 1.5$ K, reasonable water vapor profiles could be obtained when the radiance at 0.875 μm is less than 140 W cm^{-3} sr^{-1}, or the brightness at 12 μm greater than 220 K; adequate retrievals could be performed regardless of the brightness temperature values at 89 GHz.

Acknowledgments. The authors thank Drs. R. K. Kakar and T. Settle of the Office of Mission to Planet Earth, NASA Headquarters, for support of this experiment. Mr. J. Arveson and the staff of the High-Altitude Missions Branch of the NASA Ames Research Center managed the operation of the ER-2 aircraft during TOGA COARE.

REFERENCES

Falcone, V. J., and Coauthors, 1992: SSM/T-2 calibration and validation data analysis. Environmental Research Papers 1111, PL-TR-92-2293, 377 pp. [Available from Phillips Laboratory, Hanscom Air Force Base, MA 01731-5000.]

Gagliano, J. A., and J. J. McCheehy, 1981: Advanced microwave moisture sounder (AMMS) for WB-57F CCOPE mission. Georgia Institute of Technology Tech. Rep. for Project A-2904, 40 pp.

Kakar, R. K., 1983: Retrieval of clear sky moisture profiles using the 183 GHz water vapor line. *J. Climate Appl. Meteor.,* **22,** 1282–1289.

——, and B. H. Lambrigtsen, 1984: A statistical correlation method for the retrieval of atmospheric moisture profiles by microwave radiometry. *J. Climate Appl. Meteor.,* **23,** 1110–1114.

King, M. D., and Coauthors, 1996: Airborne scanning spectrometer for remote sensing of clouds, aerosol, water vapor and surface properties. *J. Atmos. Oceanic Technol.,* **13,** 777–794.

Kuo, C. C., D. H. Staelin, and P. W. Rosenkranz, 1994: Statistical iterative scheme for estimating atmospheric relative humidity profiles. *IEEE Trans. Geosci. Remote Sens.,* **32**(2), 254–260.

Lambrigtsen, B. H., and R. K. Kakar, 1985: Estimation of atmospheric moisture content from microwave radiometric measurements during CCOPE. *J. Climate Appl. Meteor.,* **24,** 266–274.

Liebe, H. J., 1989: MPM—An atmospheric millimeter-wave propagation model. *Int. J. Infrared Millimeter Waves,* **10**(6), 631–650.

——, G. A. Hufford, and T. Manabe, 1991: A model for the complex permittivity of water at frequencies below 1 THz. *Int J. Infrared Millimeter Waves,* **12**(7), 659–675.

Lutz, R., T. T. Wilheit, J. R. Wang, and R. K. Kakar, 1991: Retrieval of atmospheric water vapor profiles using radiometric measurements at 183 and 90 GHz. *IEEE Trans. Geosci. Remote Sens.,* **29**(4), 602–609.

Racette, P., R. F. Adler, J. R. Wang, A. J. Gasiewski, D. M. Jackson, and D. S. Zacharias, 1996: Millimeter-wave imaging radiometer for cloud, precipitation, and atmospheric water vapor studies. *J. Atmos. Oceanic Technol.,* **13,** 610–619.

Rosenkranz, P. W., M. J. Komichak, and D. H. Staelin, 1982: A method for estimation of atmospheric water vapor profiles by microwave radiometry. *J. Appl. Meteor.,* **21,** 1364–1370.

Schaerer, G., and T. T. Wilheit, 1979: A passive microwave technique for profiling of atmospheric water vapor. *Radio Sci.,* **14,** 371–375.

Spinhirne, J. D., and W. D. Hart, 1990: Cirrus structure and radiative parameters from airborne lidar and spectral radiometer obser-

Unauthenticated | Downloaded 05/27/24 03:17 PM UTC

vations: The 28 October 1986 study. *Mon. Wea. Rev*, **118,** 2329–2343.

——, ——, and D. L. Hlavka, 1996: Cirrus infrared parameters and shortwave and reflectance relations from observations. *J. Atmos. Sci.,* **53,** 1–20.

Wang, J. R., and L. A. Chang, 1990: Retrieval of water vapor profiles from microwave radiometric measurements near 90 and 183 GHz. *J. Appl. Meteor.,* **29,** 1006–1013.

——, and Coauthors, 1983: Profiling atmospheric water vapor by microwave radiometry. *J. Climate Appl. Meteor.,* **22,** 779–788.

——, W. C. Boncyk, and A. K. Sharma, 1993: Water vapor profiling over ocean surface from airborne 90 and 183 GHz radiometric measurements under clear and cloudy conditions. *IEEE Trans. Geosci. Remote Sens.,* **31**(4), 853–859.

——, S. H. Melfi, P. Racette, D. N. Whiteman, L. A. Chang, R. A. Ferrare, K. D. Evans, and F. J. Schmidlin, 1995: Simultaneous measurements of atmospheric water vapor with MIR, Raman lidar, and rawinsondes. *J. Appl. Meteor.,* **34,** 1595–1607.

——, P. Racette, and L. A. Chang, 1997a: MIR measurements of atmospheric water vapor profiles. *IEEE Trans. Geosci. Remote Sens.,* **35**(2), 212–223.

——, J. Zhan, and P. Racette, 1997b: Storm-associated microwave radiometric signatures in the frequency range of 90–220 GHz. *J. Atmos. Oceanic Technol.,* **14,** 13–31.

Whiteman, D. N., S. H. Melfi, and R. A. Ferrare, 1992: Raman lidar system for the measurements of water vapor and aerosols in the earth's atmosphere. *Appl. Opt.,* **31**(16), 3068–3082.

Wilheit, T. T., 1990: An algorithm for retrieving water vapor profiles in clear and cloudy atmospheres from 183 GHz radiometric measurements: Simulation studies. *J. Appl. Meteor.,* **29,** 508–515.

Unauthenticated | Downloaded 05/27/24 03:17 PM UTC